Numerical Simulations of Carbon and Nitrogen Composition–Depth Profiles Obtained by Plasma Nitrocarburization of Austenitic Stainless Steels

X. Gu, A.H. Heuer, F. Ernst, H. Kahn, G.M. Michal

Department of Materials Science and Engineering,
Case Western Reserve University, Cleveland, OH 44106

Abstract

Unusual composition–depth profiles have been observed after low-temperature nitrocarburization of austenitic stainless steels. When nitridation is performed after carburization, the carbon concentration in the nitrogen diffusion zone is reduced from ≈ 10 to ≈ 2 at%. Conversely, the carbon concentration in advance of the nitrogen diffusion zone is as high as 10 at%. This has been called a "push" effect of nitrogen on carbon, but this concept is non-physical. The profiles can be better understood from thermodynamic principles, recognizing that (i) diffusion always occurs in response to gradients in chemical potentials and (ii) the diffusivity of interstitial solutes in austenite is strongly concentration dependent, increasing dramatically with higher solute concentrations.

Parameters from the CALPHAD literature quantitatively indicate that interstitial nitrogen and carbon in austenitic stainless steel mutually increase their chemical potentials. Based on these data, we have conducted numerical simulations of composition–depth profiles that correctly account for the chemical potential gradients and the concentration dependence of the diffusion coefficients for nitrogen and carbon. The simulations predict the "push" effect observed on nitridation after carburization as well as corresponding composition–depth profiles for other scenarios, e.g., carburization followed by nitridation or simultaneous nitridation and carburization (nitrocarburization).

Background

Unusual composition–depth profiles have been observed after low-temperature carburization and nitridation of austenitic stainless steels [1-6]. In particular, when the nitridation process occurs after carburization, there is an accumulation of carbon in front of the nitrogen diffusion zone, which has been observed with a variety of composition–depth profiling techniques. Some authors describe this phenomenon as a "push" effect [2] of nitrogen on carbon.

In the present work, a quantitative explanation is provided to understand this interesting phenomenon, based upon thermodynamic analysis and numerical simulation. According to a CALPHAD-based thermodynamic computational analysis, nitrogen greatly increases the chemical potential of carbon, whose gradient is the actual driving force for carbon diffusion. In regions of high nitrogen concentration, therefore, a given chemical potential of carbon can be maintained with a lower carbon concentration. During low-temperature plasma nitridation of previously low-temperature-carburized austenitic stainless steel, this leads to a depletion of carbon within the nitrogen diffusion zone. Considering this effect and combining it with the established fact that the diffusion coefficients of both nitrogen and carbon strongly increase with concentration provides a physical explanation for the ill-defined "push" effect of nitrogen on carbon. As shown in the following, numerical simulation of the composition–depth profile based upon these principles correctly reproduces the experimentally observed profiles shown in Figure 1 [1], which includes the typical carbon (C15[C]) and nitrogen (N15[N]) concentration–depth profiles in AISI 316L stainless steel after 430°C/15h plasma carburization and nitridation as well as the carbon and nitrogen concentration–depth profiles (N15C15[C] and N15C15[N]) after 430°C/30h nitrocarburizing (15h plasma nitriding after 15h plasma carburizing).

Thermodynamic Analysis

Based upon a CALPHAD model, the austenite phase of AISI 316L can be treated as two interpenetrating FCC sublattices, one based upon Fe and substitutional solutes (Cr, Ni, Mo) and the second partially occupied by the interstitial solutes (C, N). The ratio between the total number of the substitutional sites and the interstitial sites is 1:1. Therefore, the Gibbs free energy, $G_{\mathrm{m}}^{\mathrm{FCC}}$, of one mole of formula units in this FCC phase $(\mathrm{Fe, Cr, Ni, Mo})_1(\mathrm{C, N, Va})_1$ can be expressed as

$$\begin{aligned}
G_{\mathrm{m}}^{\mathrm{FCC}} = {} & Y_{\mathrm{Fe}}Y_{\mathrm{C}}\,{}^{\mathrm{o}}G_{\mathrm{Fe:C}}^{\mathrm{HFCC}} + Y_{\mathrm{Fe}}Y_{\mathrm{N}}\,{}^{\mathrm{o}}G_{\mathrm{Fe:N}}^{\mathrm{HFCC}} + Y_{\mathrm{Fe}}Y_{\mathrm{Va}}\,{}^{\mathrm{o}}G_{\mathrm{Fe:Va}}^{\mathrm{HFCC}} \\
& + Y_{\mathrm{Cr}}Y_{\mathrm{C}}\,{}^{\mathrm{o}}G_{\mathrm{Cr:C}}^{\mathrm{HFCC}} + Y_{\mathrm{Cr}}Y_{\mathrm{N}}\,{}^{\mathrm{o}}G_{\mathrm{Cr:N}}^{\mathrm{HFCC}} + Y_{\mathrm{Cr}}Y_{\mathrm{Va}}\,{}^{\mathrm{o}}G_{\mathrm{Cr:Va}}^{\mathrm{HFCC}} \\
& + Y_{\mathrm{Ni}}Y_{\mathrm{C}}\,{}^{\mathrm{o}}G_{\mathrm{Ni:C}}^{\mathrm{HFCC}} + Y_{\mathrm{Ni}}Y_{\mathrm{N}}\,{}^{\mathrm{o}}G_{\mathrm{Ni:N}}^{\mathrm{HFCC}} + Y_{\mathrm{Ni}}Y_{\mathrm{Va}}\,{}^{\mathrm{o}}G_{\mathrm{Ni:Va}}^{\mathrm{HFCC}} \\
& + Y_{\mathrm{Mo}}Y_{\mathrm{C}}\,{}^{\mathrm{o}}G_{\mathrm{Mo:C}}^{\mathrm{HFCC}} + Y_{\mathrm{Mo}}Y_{\mathrm{N}}\,{}^{\mathrm{o}}G_{\mathrm{Mo:N}}^{\mathrm{HFCC}} + Y_{\mathrm{Mo}}Y_{\mathrm{Va}}\,{}^{\mathrm{o}}G_{\mathrm{Mo:Va}}^{\mathrm{HFCC}} \\
& + \mathrm{R}T\left(Y_{\mathrm{Fe}}\ln Y_{\mathrm{Fe}} + Y_{\mathrm{Cr}}\ln Y_{\mathrm{Cr}} + Y_{\mathrm{Ni}}\ln Y_{\mathrm{Ni}} + Y_{\mathrm{Mo}}\ln Y_{\mathrm{Mo}} + Y_{\mathrm{C}}\ln Y_{\mathrm{C}} + Y_{\mathrm{N}}\ln Y_{\mathrm{N}} + Y_{\mathrm{Va}}\ln Y_{\mathrm{Va}}\right) \\
& + G_{\mathrm{m}}^{\mathrm{excess}} + G_{\mathrm{m}}^{\mathrm{mag.}},
\end{aligned} \tag{1}$$

where Va represents a vacant interstitial site, Y_i are site fractions, and RT has its usual meaning.

According to the CALPHAD model, the molar Gibbs free energy is the sum of the mechanical mixture of all the end members in the FCC phase, the ideal entropy, the excess energy of mixing and the magnetic contribution. In Eq. (1), the first four lines represent the mechanical mixture of all the end members. The fifth line contains the ideal entropy term. The excess energy of mixing is expressed as

$$\begin{aligned}
G_{\mathrm{m}}^{\mathrm{excess}} = {} & Y_{\mathrm{C}}Y_{\mathrm{Va}}\left(Y_{\mathrm{Fe}}\,{}^{0}L_{\mathrm{Fe:C,Va}}^{\mathrm{FCC}} + Y_{\mathrm{Cr}}\,{}^{0}L_{\mathrm{Cr:C,Va}}^{\mathrm{FCC}} + Y_{\mathrm{Ni}}\,{}^{0}L_{\mathrm{Ni:C,Va}}^{\mathrm{FCC}} + Y_{\mathrm{Mo}}\,{}^{0}L_{\mathrm{Mo:C,Va}}^{\mathrm{FCC}}\right) \\
& + Y_{\mathrm{N}}Y_{\mathrm{Va}}\left(Y_{\mathrm{Fe}}\,{}^{0}L_{\mathrm{Fe:N,Va}}^{\mathrm{FCC}} + Y_{\mathrm{Cr}}\,{}^{0}L_{\mathrm{Cr:N,Va}}^{\mathrm{FCC}} + Y_{\mathrm{Mo}}\,{}^{0}L_{\mathrm{Mo:N,Va}}^{\mathrm{FCC}}\right) \\
& + Y_{\mathrm{Fe}}Y_{\mathrm{C}}Y_{\mathrm{N}}\,{}^{0}L_{\mathrm{Fe:C,N}}^{\mathrm{FCC}} + Y_{\mathrm{Cr}}Y_{\mathrm{Fe}}Y_{\mathrm{C}}\,{}^{0}L_{\mathrm{Cr,Fe:C}}^{\mathrm{FCC}} + Y_{\mathrm{Cr}}Y_{\mathrm{Fe}}Y_{\mathrm{N}}\left({}^{0}L_{\mathrm{Cr,Fe:N}}^{\mathrm{FCC}} + {}^{1}L_{\mathrm{Cr,Fe:N}}^{\mathrm{FCC}}\left(Y_{\mathrm{Cr}} - Y_{\mathrm{Fe}}\right)\right) \\
& + Y_{\mathrm{Cr}}Y_{\mathrm{Fe}}Y_{\mathrm{Va}}\left({}^{0}L_{\mathrm{Cr,Fe:Va}}^{\mathrm{FCC}} + {}^{1}L_{\mathrm{Cr,Fe:Va}}^{\mathrm{FCC}}\left(Y_{\mathrm{Cr}} - Y_{\mathrm{Fe}}\right)\right) + Y_{\mathrm{Cr}}Y_{\mathrm{Fe}}Y_{\mathrm{N}}Y_{\mathrm{Va}}\,{}^{0}L_{\mathrm{Cr,Fe:N,Va}}^{\mathrm{FCC}} \\
& + Y_{\mathrm{Fe}}Y_{\mathrm{Ni}}Y_{\mathrm{C}}\left({}^{0}L_{\mathrm{Fe,Ni:C}}^{\mathrm{FCC}} + {}^{1}L_{\mathrm{Fe,Ni:C}}^{\mathrm{FCC}}\left(Y_{\mathrm{Fe}} - Y_{\mathrm{Ni}}\right)\right) + Y_{\mathrm{Fe}}Y_{\mathrm{Ni}}Y_{\mathrm{N}}\left({}^{0}L_{\mathrm{Fe,Ni:N}}^{\mathrm{FCC}} + {}^{1}L_{\mathrm{Fe,Ni:N}}^{\mathrm{FCC}}\left(Y_{\mathrm{Fe}} - Y_{\mathrm{Ni}}\right)\right) \\
& + Y_{\mathrm{Fe}}Y_{\mathrm{Ni}}Y_{\mathrm{Va}}\left({}^{0}L_{\mathrm{Fe,Ni:Va}}^{\mathrm{FCC}} + {}^{1}L_{\mathrm{Fe,Ni:Va}}^{\mathrm{FCC}}\left(Y_{\mathrm{Fe}} - Y_{\mathrm{Ni}}\right) + {}^{2}L_{\mathrm{Fe,Ni:Va}}^{\mathrm{FCC}}\left(Y_{\mathrm{Fe}} - Y_{\mathrm{Ni}}\right)^{2}\right) \qquad (2) \\
& + Y_{\mathrm{Cr}}Y_{\mathrm{Fe}}Y_{\mathrm{Ni}}Y_{\mathrm{C}}\,{}^{0}L_{\mathrm{Cr,Fe,Ni:C}}^{\mathrm{FCC}} + Y_{\mathrm{Cr}}Y_{\mathrm{Fe}}Y_{\mathrm{Ni}}Y_{\mathrm{Va}}\,{}^{0}L_{\mathrm{Cr,Fe,Ni:Va}}^{\mathrm{FCC}} + Y_{\mathrm{Fe}}Y_{\mathrm{Mo}}Y_{\mathrm{C}}\,{}^{0}L_{\mathrm{Fe,Mo:C}}^{\mathrm{FCC}} \\
& + Y_{\mathrm{Fe}}Y_{\mathrm{Mo}}Y_{\mathrm{Va}}\,{}^{0}L_{\mathrm{Fe,Mo:Va}}^{\mathrm{FCC}} + Y_{\mathrm{Cr}}Y_{\mathrm{Ni}}Y_{\mathrm{C}}\,{}^{0}L_{\mathrm{Cr,Ni:C}}^{\mathrm{FCC}} + Y_{\mathrm{Cr}}Y_{\mathrm{Ni}}Y_{\mathrm{Va}}\left({}^{0}L_{\mathrm{Cr,Ni:Va}}^{\mathrm{FCC}} + {}^{1}L_{\mathrm{Cr,Ni:Va}}^{\mathrm{FCC}}\left(Y_{\mathrm{Cr}} - Y_{\mathrm{Ni}}\right)\right) \\
& + Y_{\mathrm{Cr}}Y_{\mathrm{Ni}}Y_{\mathrm{N}}Y_{\mathrm{Va}}\,{}^{0}L_{\mathrm{Cr,Ni:N,Va}}^{\mathrm{FCC}} + Y_{\mathrm{Cr}}Y_{\mathrm{Mo}}Y_{\mathrm{N}}\,{}^{0}L_{\mathrm{Cr,Mo:N}}^{\mathrm{FCC}} \\
& + Y_{\mathrm{Cr}}Y_{\mathrm{Mo}}Y_{\mathrm{Va}}\left({}^{0}L_{\mathrm{Cr,Mo:Va}}^{\mathrm{FCC}} + {}^{1}L_{\mathrm{Cr,Mo:Va}}^{\mathrm{FCC}}\left(Y_{\mathrm{Cr}} - Y_{\mathrm{Mo}}\right)\right) \\
& + Y_{\mathrm{Mo}}Y_{\mathrm{Ni}}Y_{\mathrm{Va}}\left({}^{0}L_{\mathrm{Mo,Ni:Va}}^{\mathrm{FCC}} + {}^{1}L_{\mathrm{Mo,Ni:Va}}^{\mathrm{FCC}}\left(Y_{\mathrm{Mo}} - Y_{\mathrm{Ni}}\right)\right),
\end{aligned}$$

where ${}^{n}L_{\mathrm{i}}^{\mathrm{FCC}}$ are the CALPHAD interaction parameters. The contribution of ferromagnetism to the Gibbs free energy of the FCC phase can be ignored at the temperature where carburization and nitridation treatments are performed.

The chemical potentials of the interstitial elements carbon and nitrogen are also well defined in the CALPHAD model:

$$\mu_{\mathrm{C}}^{\mathrm{FCC}} = \frac{\partial G_{\mathrm{m}}^{\mathrm{FCC}}}{\partial Y_{\mathrm{C}}} - \frac{\partial G_{\mathrm{m}}^{\mathrm{FCC}}}{\partial Y_{\mathrm{Va}}} \quad , \qquad (3)$$

$$\mu_{\mathrm{N}}^{\mathrm{FCC}} = \frac{\partial G_{\mathrm{m}}^{\mathrm{FCC}}}{\partial Y_{\mathrm{N}}} - \frac{\partial G_{\mathrm{m}}^{\mathrm{FCC}}}{\partial Y_{\mathrm{Va}}} \qquad (4)$$

Accordingly, the chemical potentials of carbon and nitrogen in AISI 316L stainless steel with a nominal composition Fe–18Cr–12Ni–2Mo (in wt%) at 430°C can be defined based upon the relevant thermodynamic parameters recorded in the CALPHAD literature [7-17].

The chemical potential of carbon relative to graphite in AISI 316L stainless steel at 430°C is

$$\mu_{\mathrm{C}}^{\mathrm{FCC}} - {}^{\mathrm{o}}G_{\mathrm{C}}^{\mathrm{gra}} = K_1 Y_{\mathrm{C}} + K_2 Y_{\mathrm{N}} + K_3 \ln \frac{Y_{\mathrm{C}}}{1 - Y_{\mathrm{C}} - Y_{\mathrm{N}}} + K_4 \tag{5}$$

with K_1 = 52.42 kJ/mol, K_2 = 55.29 kJ/mol, K_3 = 5.85 kJ/mol, and K_4 = 10.41 kJ/mol. The chemical potential of carbon relative to graphite is plotted in Figure 2 as a function of the atom fractions of carbon and nitrogen, based upon the conversion $X_{\mathrm{C}} = Y_{\mathrm{C}} / (1+Y_{\mathrm{C}}+Y_{\mathrm{N}})$ and $X_{\mathrm{N}} = Y_{\mathrm{N}} / (1+Y_{\mathrm{N}}+Y_{\mathrm{C}})$ for an FCC phase. Figure 2 illustrates that nitrogen greatly increases the chemical potential of carbon in austenite. For example, consider that the chemical potential of 2 at% carbon in AISI 316L is about – 11 kJ/mol relative to graphite. After introducing about 18 at% nitrogen into the system, the chemical potential of 2 at% carbon is raised to about 4 kJ/mol relative to graphite. This chemical potential level is equivalent to that of about 10 at% carbon when there is no nitrogen in the system. We denote the actual carbon fraction after the introduction of nitrogen as $X_{\mathrm{C}}^{\mathrm{a}}$ and the "effective" carbon fraction with the same chemical potential absent nitrogen as $X_{\mathrm{C}}^{\mathrm{e}}$. The influence of nitrogen during plasma nitriding is to maintain a driving force for the inward diffusion of carbon through increasing the chemical potential gradient of carbon. It is this effect that results in what appears to be nitrogen "pushing" the carbon ahead of the nitrogen diffusion zone. Inward diffusion of nitrogen provides an increased chemical potential gradient for carbon, without any increase in the surface concentration of carbon.

Similarly, carbon influences the chemical potential of nitrogen. By employing the same analysis, the chemical potential of nitrogen relative to one half of the Gibbs free energy of diatomic nitrogen gas in AISI 316L stainless steel at 430°C is

$$\mu_{\mathrm{N}}^{\mathrm{FCC}} - 0.5\,{}^{\mathrm{o}}G_{\mathrm{N}_2}^{\mathrm{gas}} = K_5 Y_{\mathrm{N}} + K_2 Y_{\mathrm{C}} + K_3 \ln \frac{Y_{\mathrm{N}}}{1 - Y_{\mathrm{N}} - Y_{\mathrm{C}}} + K_6 \tag{6}$$

with $K5$ = 87.46 kJ/mol, and K_6 = – 22.18 kJ/mol. The chemical potential of nitrogen relative to diatomic nitrogen gas is plotted in Figure 3 as a function of a carbon content for various nitrogen levels. Figure 3 reveals that carbon greatly increases the chemical potential of nitrogen. Corresponding to the terminology for carbon, we define the actual nitrogen fraction with carbon in the system as $X_{\mathrm{N}}^{\mathrm{a}}$ and the "effective" nitrogen content corresponding to the same chemical potential absent carbon as $X_{\mathrm{N}}^{\mathrm{e}}$.

According to Eqs. (5) and (6), the magnitudes of the mutually enhanced carbon and nitrogen chemical potentials are actually the same. However, the influence of carbon on the chemical potential of nitrogen is smaller than that of nitrogen on the chemical potential of carbon. This is because for AISI 316L – according to the results of carburization and nitridation treatments [1] – the maximum nitrogen concentration is greater than the maximum carbon concentration. Eqs. (5) and (6) have been utilized in the numerical simulations of composition–depth profiles, which are presented next.

Numerical Simulation of Composition–Depth Profiles

The numerical simulations were based upon the well-known finite difference method [18], where Fick's second law is discretized as a finite difference approximation in the dimensions of processing time t (s) and penetration depth x (μm). The Crank–Nicholson algorithm [18] was employed for these computations. Regarding the boundary conditions at the alloy surface, the high efficiency of the surface activation treatment that removes the Cr_2O_3-rich passivating film during plasma treatment was accounted for by assuming that the mass transfer coefficient at the gas–metal interface is infinite. Effectively, nitrogen and carbon concentrations at the very surface of the alloy reach their paraequilibrium solubility limit at the inception of the treatment.

(1) Concentration Dependence of the Diffusion Coefficients

The convex shape of the carbon and nitrogen concentration–depth profiles that develop during plasma carburization and nitridation can be successfully modeled by recognizing the concentration dependence of the diffusion coefficients of carbon and nitrogen in stainless steels. From Figure 1, the carbon profile for the sample carburized at 430°C (C15[C]) is convex upward, which is very different from the conventional error-function solution to the diffusion equation with a constant diffusion coefficient [19]. The diffusion coefficient strongly increases with the carbon concentration, particularly when the carbon content is as high as 10 at%. The nitrogen profile for the sample nitrided at 430°C (N15[N]) also has a convex shape, indicating that the diffusion coefficient of nitrogen also strongly increases with concentration. This type of concentration-dependent diffusion coefficient can be described by an exponential function [19]:

$$\tilde{D}/D = \mathrm{Exp}\left[k \frac{X}{X_{\max}} \right] , \qquad (7)$$

where $\tilde{D}$ is the concentration-dependent diffusion coefficient, D is the diffusion coefficient at infinite dilution, and X and $X_{\max}$ are the actual concentration and the

maximum possible concentration. The parameter k controls the magnitude of the concentration dependence. For example, when X is X_{max}, $\tilde{D}$ is e^k times D. Figure 4 shows a classical set [20] of calculated and normalized concentration-depth profiles for various values of e^k. When $e^k = 1$, $\tilde{D}$ is independent of concentration, so the profile has the form of the error function solution. When k increases, the concentration dependence of the diffusion coefficient also increases and the profile becomes upwardly convex. When e^k increases to several hundred, the profile appears to have a plateau with a very steep leading edge.

(2) Simulation of a Carbon Depth Profile for Carburization at 430°C

A simulated carbon profile obtained by finite difference modeling for a 430°C /15h carburization experiment is shown in Figure 5. The maximum carbon concentration at the gas–metal interface was assumed to be 10 at% [1]. D for carbon in AISI 316L stainless steel, $4.5 \cdot 10^{-5}$ $\mu m^2/s$ at 430°C was obtained from Agarwala *et al.* [21].

The best fit corresponds to $k \approx 5$, implying that the diffusion coefficient of carbon at a 10 at% carbon content is about 145 times the diffusion coefficient at infinite carbon dilution. The fit is excellent, except for the data at low carbon concentrations. That discrepancy is most likely due to an extension of the carbon distribution parallel to the direction of sputtering inherent in the GDOES technique used to measure the carbon concentration–depth profile [1].

(3) Simulation of a Nitrogen Concentration–Depth Profile for 430°C Nitriding

A similarly good fit was obtained for a nitrogen depth profile generated by plasma nitriding at 430°C/15h, as shown in Figure 6. The maximum concentration at the gas–metal interface was assumed to be 17 at% [1]. An average of three values of D for nitrogen in AISI 316L stainless steel at 430°C found in the literature [22, 23, 24], $2.8 \cdot 10^{-5}$ $\mu m^2/s$, was used for the simulations.

The best fit for k in Figure 6 was 4.2, i.e., the diffusion coefficient of nitrogen at a 17 at% nitrogen content is ≈ 67 times the diffusion coefficient at infinite dilution, less marked than for carbon at the same concentration. The diffusion coefficient of nitrogen at 10 at% based upon Eq. (7) is 12.2 D. Given that D_N / D_C is 0.6, carbon diffuses about 20 times faster than nitrogen at the 10 at% concentration level at 430°C.

(4) Simulation of Carbon and Nitrogen Concentration–Depth Profiles for 430°C Nitrocarburization

To simulate nitrocarburization, we maintained the simulation parameters employed for sole carburization and sole nitridation treatments except for the following two points:

Firstly, for the simulation of the carbon depth profile during plasma nitriding, the gas–metal interface was assumed to be impermeable to carbon. This is reasonable because during nitridation, (i) no carbon can enter the metal through the surface because there is no carbon in the nitriding atmosphere, and (ii), no carbon can escape through the surface because carbon desorption is extremely difficult under these conditions.

Secondly, the *k* parameter for carbon during plasma nitridation should be higher than the value used for Figure 5, because the effective-carbon concentration increases to a much higher level due to the increased chemical potential of carbon. It is difficult to predict the exact value of *k* at the higher effective-carbon concentration level, which can be up to 18 at% based upon the calculation shown by Eq. (5). A variety of *k* values for carbon were tried in the simulation, and the *k* value of 6.5 for carbon concentrations up to 18 at% yielded the most satisfactory fit.

The simulation started with the carbon concentration–depth profile shown in Figure 5. How the carbon and nitrogen concentration–depth profiles change within the first minute is demonstrated in order to show the computational logic used for the simulation. There were a total of six calculations for each time step, as shown in Figure 7.

Figure 7(a) shows the first step. Plasma nitridation starts and the effective-nitrogen concentration $X_{\mathrm{N}}^{\mathrm{e}}$, representing the chemical potential of nitrogen, equilibrates with the maximum possible nitrogen concentration of 17 at% at the gas–metal interface as determined by the nitrogen activity in the nitriding gas atmosphere. Then the effective nitrogen diffuses based upon the highly concentration-dependent diffusion coefficient of nitrogen used to produce Figure 6. The simulated effective-nitrogen concentration–depth profile after the diffusion for one time step is shown in Figure 7(b). A fixed boundary condition was used during this step.

Figure 7(c) shows the third step. Because carbon can increase the chemical potential of nitrogen, the actual nitrogen solubility in AISI 316L stainless steel under a given nitrogen activity decreases, and the actual nitrogen concentration–depth profile was computed based upon the current values of $X_{\mathrm{C}}^{\mathrm{a}}$ and $X_{\mathrm{N}}^{\mathrm{e}}$, according to Eq. (6). Because nitrogen also greatly increases the chemical potential of carbon, the effective-carbon concentration–depth profile was computed based upon the actual concentrations of $X_{\mathrm{N}}^{\mathrm{a}}$ and $X_{\mathrm{C}}^{\mathrm{a}}$, according to Eq. (5). The computed profile of the effective-carbon concentration is shown in Figure 7(d).

Figure 7(e) shows the fifth step. Carbon diffuses based upon a highly concentration-dependent diffusion coefficient, and the profile was simulated under the boundary condition of an impermeable solid–gas interface, as described earlier. The k parameter used in this simulation is 6.5, which as already discussed is larger than the value of 5 obtained from Figure 5. Then the actual carbon concentration–depth profile was computed based upon the current values of $X_{\mathrm{C}}^{\mathrm{e}}$ and $X_{\mathrm{N}}^{\mathrm{a}}$, according to Eq. (5) again. The computed profile of the actual carbon concentration is shown in Figure 7(f).

The actual carbon and nitrogen concentration–depth profiles at the end of the first minute of processing are shown in Figure 7(g). Due to the highly concentration-dependent diffusivity of carbon, the actual carbon concentration near the surface decreases to a very low level, while a peak develops along the actual carbon concentration profile. The actual carbon and nitrogen concentration–depth profiles shown in Figure 7(g) were taken as the initial concentration–depth profiles for the next time step and then repeated until the end of the simulation for the 15-hour plasma nitridation process.

Figure 8 shows the simulated concentration–depth profiles $X_{\mathrm{C}}^{\mathrm{a}}$, $X_{\mathrm{C}}^{\mathrm{e}}$, and $X_{\mathrm{N}}^{\mathrm{a}}$ for total elapsed times of 5 minutes, 10 minutes, 20 minutes, 30 minutes, 1 hour, 3 hours, 5 hours and 10 hours of plasma nitridation treatment. Obviously, the actual peak along the carbon concentration–depth profile generated during the beginning of the treatment is gradually homogenized due to carbon diffusion, and after about 1 h, a smooth curve develops.

Figure 9(a) shows the simulated final concentration–depth profiles $X_{\mathrm{C}}^{\mathrm{a}}$, $X_{\mathrm{C}}^{\mathrm{e}}$ and $X_{\mathrm{N}}^{\mathrm{a}}$. Due to the large amount of nitrogen introduced during the plasma nitridation treatment, the effective-carbon concentration–depth profile, representing the chemical potential of carbon, develops as a very smooth and monotonously decreasing curve, although the actual carbon concentration seems to be depleted within the nitrogen diffusion zone. In Figure 9(b), it is obvious that there is a good agreement between the simulated carbon concentration–depth profiles and the experimental results displayed in Figure 1. The general shape of the actual-carbon concentration–depth profile agrees with the experimental profile, although the fit is not perfect. However, considering the difficulties in obtaining the experimental profiles using the GDOES technique and the assumptions and approximations made during the simulation, the fit is satisfactory.

The smooth effective-carbon-concentration–depth profile demonstrates that the large nitrogen content introduced by plasma nitridation provides a significant driving force for carbon diffusion, i.e., the chemical potential gradient of carbon during the plasma nitridation process, rather than carbon being "pushed" ahead of the nitrogen diffusion zone. It also should be noted that with the similar influence of carbon on the

nitrogen chemical potential gradient, the nitrogen profile becomes a little flatter compared with the original nitrogen concentration–depth profile. In addition, the maximum concentration of nitrogen at the surface decreases a little due to the modest amount of carbon present in the nitrogen diffusion zone. These results also are in excellent agreements with the experimental concentration–depth profiles shown in Figure 1.

Figure 10 shows the final chemical potential profiles of carbon calculated using Eq. (3) applied to the CALPHAD model. Figure 10(a) is based upon the carbon and nitrogen concentration values taken from the experimentally determined concentration–depth profiles N15C15[C] and N15C15[N] displayed in Figure 1, while Figure 10(b) lies on the carbon and nitrogen concentrations from the simulated concentration–depth profiles contained in Figure 9(b).

Both profiles in Figure 10 have some relative error. The chemical potential profile for carbon has a valley at a depth of around 5 μm in Figure 10(a), and the chemical potential profile for carbon has a small hump at a similar position in Figure 10(b). Possible uncertainties in the experimental depth profiles have already been mentioned. The simulation error is mainly due to the linearization of the relationship between the effective concentration–depth profile and the actual concentration–depth profile. According to the above analyses, it is clear that the final chemical potential profile of carbon should be similar to the $X_{\mathrm{C}}^{\mathrm{e}}$ curve in Figure 9(a).

Simulation Predictions

Similar simulations were used to predict the other two types of processing "recipes": (1) 15-h plasma nitridation followed by 15-h plasma carburization at 430°C, and (2) 30-h simultaneous plasma nitrocarburizing process at 430°C. The simulation for a 15-h plasma nitridation followed by a 15-h plasma carburization at 430°C was based upon essentially the same set of parameters defined and employed in the previous simulation for a 15-h plasma carburization followed by a 15-h plasma nitridation at 430°C. The computational logic was adjusted accordingly based upon the different order of the plasma carburization and plasma nitridation processes. Similarly, an impermeable boundary condition was employed at the free surface for the diffusion of nitrogen during plasma carburization, and the value of the k parameter for nitrogen was empirically determined to be 5 at nitrogen concentrations up to 19 at%, which is higher than the value of 4.2 at nitrogen concentrations up to 17 at%, used to produce Figure 6. The simulated profiles of the actual carbon and nitrogen concentrations are shown in Figure 11.

Figure 11 shows that the penetration depth of the carbon profile is shallower, and the penetration depth of the nitrogen profile is greater, compared with the carbon and nitrogen profiles contained in Figure 9. This is reasonable because nitrogen diffuses for 15 more hours and carbon diffuses for 15 fewer hours for the treatment represented in Figure 11 compared to the one shown in Figure 9. In Figure 11, the surface concentration of nitrogen has decreased to about 10 at% during the subsequent plasma carburization, due to the highly concentration-dependent diffusion coefficient of nitrogen. The carbon concentration within the nitrogen diffusion zone rose only to the 3 or 4 at% level. That occurred because the actual carbon concentration had to decrease to maintain the chemical potential of carbon determined by the carburizing gas atmosphere in the presence of the large amount of nitrogen introduced before the carburization treatment. Carbon is able to increase to a higher concentration level ahead of the nitrogen diffusion zone and develops a shape similar to that observed in Figure 9, although this tendency is not so obvious in Figure 11 considering the restriction on the length of time for diffusion.

In the simulation for 30-h simultaneous plasma nitrocarburizing at 430°C displayed in Figure 12, the plasma carburization and the plasma nitridation proceeded at the same time. Therefore, the chemical potentials of carbon and nitrogen were both determined by the activities of carbon and nitrogen in the carbonitriding gas atmosphere, which were the same as those employed during the individual carburization and nitridation processes used to create Figure 5 and Figure 6 and ignoring the mutual influence on the activities of carbon and nitrogen due to the mixing of the treatment gases.

In Figure 12, the penetration depths of both carbon and nitrogen are larger compared with the penetration depths displayed in Figure 9. In addition, the shapes of the carbon and nitrogen depth profiles seem very similar to those displayed in Figure 9. The larger diffusion coefficient of carbon than nitrogen caused carbon to develop a peak in its concentration–depth profile ahead of the nitrogen diffusion zone at the very beginning of the simultaneous nitrocarburizing process.

Figure 13 shows the concentration–depth profiles of the actual total amount of carbon and nitrogen, produced by the three different processes at 430°C: (a) 15-h plasma carburization followed by 15-h plasma nitridation, (b) 15-h plasma nitridation followed by 15-h plasma carburization, and (c) 30-h simultaneous plasma nitrocarburizing. The surface concentrations of the total amount of carbon and nitrogen are similar for process (a) and process (c), and both higher than that produced by process (b). This is due to the nitrogen concentration decreasing significantly during the plasma carburization in process (b). All three processes produced similar low carbon concentrations at the surface.

The deepest total penetration with carbon and nitrogen is obtained for process (c). The shallowest penetration among these three processes results from process (b). This is mainly because carbon diffuses faster than nitrogen under the conditions of these

simulations, and carbon diffuses for 30 h in both process (a) and process (c), while nitrogen diffuses for 30 h in process (b). The shapes of the profiles in Figure 13 should be interpreted qualitatively due to the assumptions and approximations made to obtain the simulations. A more accurate quantification of these simulations warrants further exploration.

Conclusion

The unusual shape of a carbon concentration–depth profile generated by low-temperature plasma nitrocarburizing can be explained by classical diffusion theory, recognizing the concentration dependence of both carbon and nitrogen diffusivities in stainless steels. The large nitrogen concentration introduced by plasma nitridation significant enhances the chemical potential of carbon. This generates a chemical potential gradient that provides a driving force for carbon to diffuse counter to its concentration gradient to reach regions of lower nitrogen concentration.

Reference

[1]. H. Dong, *International Materials Reviews*, Vol. 55, No. 2, pp. 65-98, 2010.

[2]. M. Tsujikawa, N. Yamauchi, N. Ueda, T. Sone and Y. Hirose, *Surface and Coatings Technology*, Vol. 193, pp. 309-313, 2005.

[3]. N. Yamauchi, N. Ueda, K. Demizu, A. Okamoto and T. Sone, *Stainless Steel 2000: Proceeding of an International Current Status Seminar on Thermochemical Surface Engineering of Stainless Steel*, Maney Publishing, London, pp. 247-261, 2001.

[4]. M. Higashi, K. Shinkawa and K. Kurosawa, *Stainless Steel 2000: Proceeding of an International Current Status Seminar on Thermochemical Surface Engineering of Stainless Steel*, Maney Publishing, London, pp. 407-413, 2001.

[5]. D.L. Williamson, P.J. Wilbur, F.R. Fickett and S. Parascandola, *Stainless Steel 2000: Proceeding of an International Current Status Seminar on Thermochemical Surface Engineering of Stainless Steel*, Maney Publishing, London, pp. 333-352, 2001.

[6]. M.P. Fewell, P. Garlick, J.M. Priest, P.T. Burke, N. Dytlewski, K.E. Prince, K.T. Short, R.G. Elliman, H. Timmers, T.D.M. Weijers and B. Gong, *Stainless Steel 2000: Proceeding of an International Current Status Seminar on Thermochemical Surface Engineering of Stainless Steel*, Maney Publishing, London, pp. 177-200, 2001.

[7]. B. Lee, *CALPHAD*, Vol. 16, No. 2, pp. 121-149, 1992.

[8]. J. Bratberg and K. Frisk, *Metallurgical and Materials Transactions A*, Vol. 35A, pp. 3649-3663, 2004.

[9]. J. Andersson, *CALPHAD*, Vol. 12, No. 1, pp. 9-23, 1988.

[10]. K. Frisk, *Metallurgical Transactions A*, Vol. 21A, pp. 2477-2488, 1990.

[11]. K. Frisk, *Zeitschrift fur Metallkunde*, Vol. 82, No. 1, pp. 59-66, 1991.

[12]. K. Frisk, *CALPHAD*, Vol. 15, No. 1, pp. 79-106, 1991.

[13]. H. Du, *Journal of Phase Equilibira*, Vol. 14, No. 6, pp. 682-693, 1993.

[14]. M. Hillert and C. Qiu, *Metallurgical Transactions A*, Vol. 22A, pp. 2187-2198, 1991.

[15]. K. Frisk, *Zeitschrift fur Metallkunde*, Vol. 82, No. 2, pp. 108-117, 1991.

[16]. C. Qiu, *CALPHAD*, Vol. 16, No. 3, pp. 281-289, 1992.

[17]. K. Frisk, *CALPHAD*, Vol. 14, No. 3, pp. 311-320, 1990.

[18]. M. Necati Özisik, *Finite Difference Methods in Heat Transfer*, CRC Press Inc., Boca Raton, Florida, U.S.A., pp. 118-120, 1994.

[19]. F. Ernst, A. Avishai, H. Kahn, X. Gu, G.M. Michal and A.H. Heuer, *Metallurgical and Materials Transactions A*, Vol. 40A, pp. 1768-1780, 2009.

[20]. J. Crank, *The Mathematics of Diffusion*, Clarendon Press, Oxford, 1956.

[21]. R.P. Agarwala, M.C. Naik, M.S. Anand and A.R. Paul, *Journal of Nuclear Materials*, Vol. 36, pp. 41-47, 1970.

[22]. J. Hirvonen and A. Anttila, *Appl. Phys. Lett*., Vol. 46, pp. 835-836, 1985.

[23]. W. Anwand, S. Parascandola, E. Richter, G. Brauer, P.G. Coleman and W. Möller, *Nucl. Instr. Meth. Phys. Res. B*, Vol. 768, pp. 136-138, 1998.

[24]. T.L. Christiansen and M.A.J. Somers, *Int. J. Mat. Res*., Vol. 99 (9), pp. 999-1005, 2008.

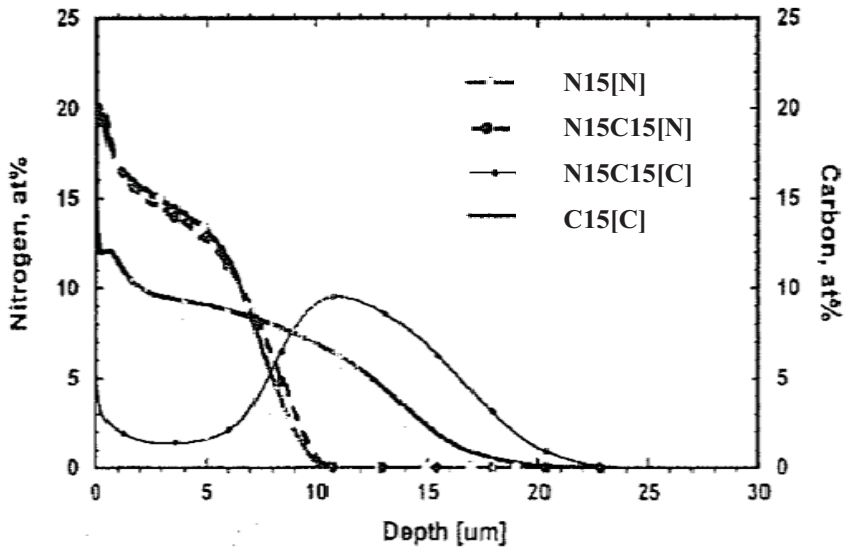

Figure 1. Typical concentration–depth profiles of nitrogen and carbon in AISI 316L stainless steel: nitrogen profile for 430°C/15h nitridation (N15[N]), carbon profile for 430°C/15h carburization (C15[C]), and nitrogen and carbon profiles for 430°C/30h nitrocarburization (N15C15[N] and N15C15[C]).

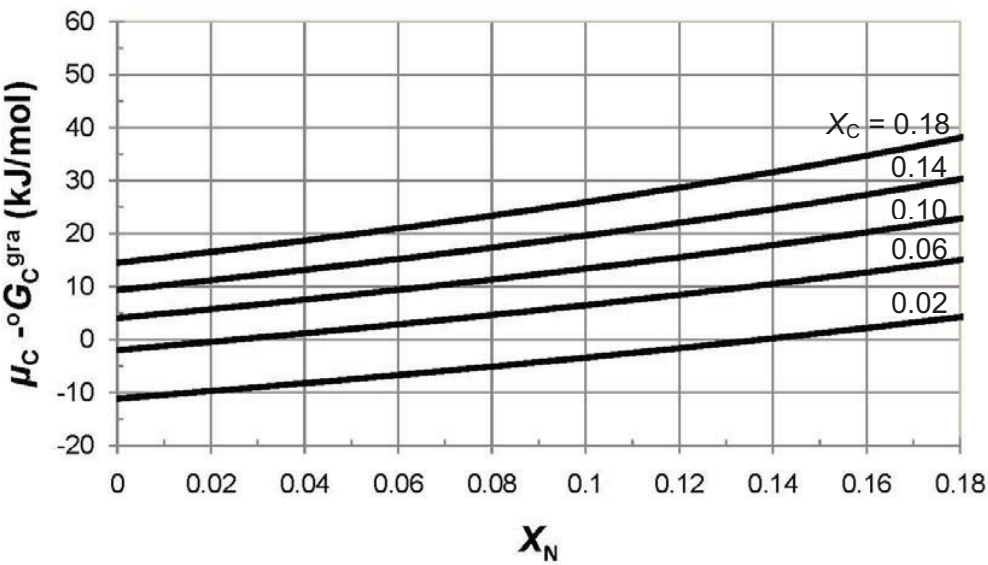

Figure 2. The chemical potential of carbon relative to graphite in AISI 316L stainless steel at 430°C. The curves correspond to the chemical potentials of carbon for a series of carbon concentrations 2-18 at% (spacing as 4 at% each).

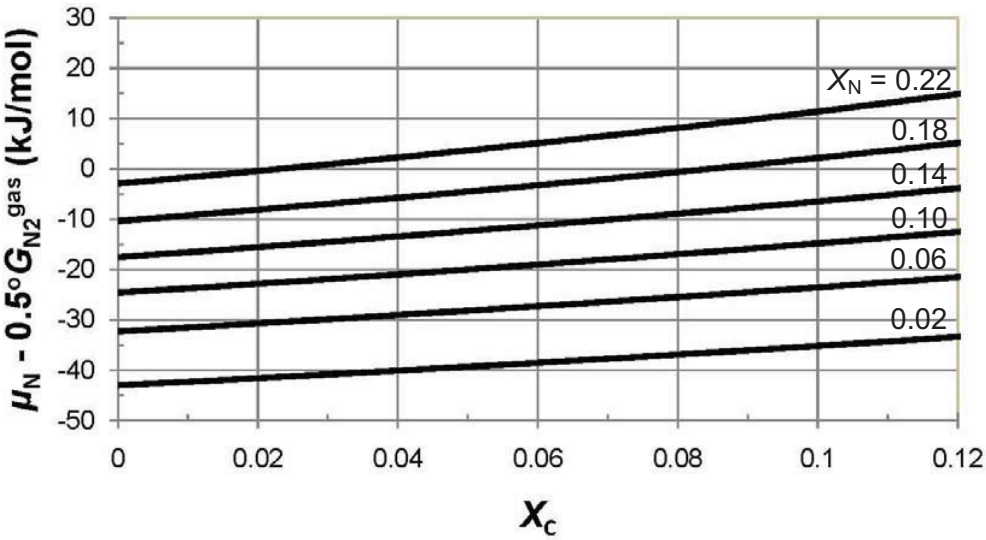

Figure 3. The chemical potential of nitrogen relative to one half of the Gibbs free energy of diatomic nitrogen gas in AISI 316L stainless steel at 430°C. The curves correspond to the chemical potentials of nitrogen for a series of nitrogen concentrations 2-22 at% (spacing as 4 at% each).

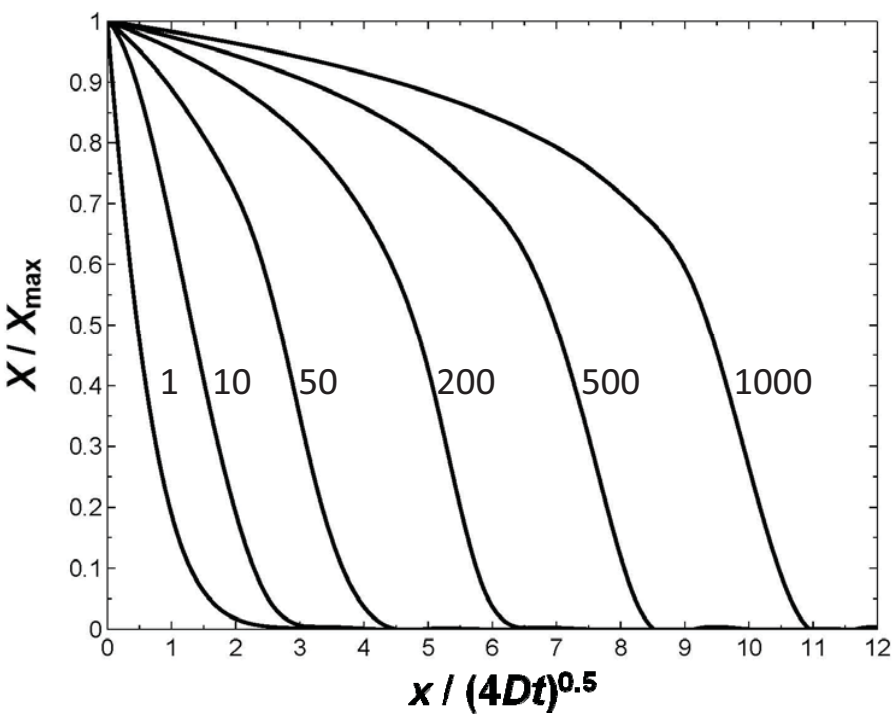

Figure 4. Calculated profiles for the normalized concentration dependence of the diffusion coefficient for various values of e^k.

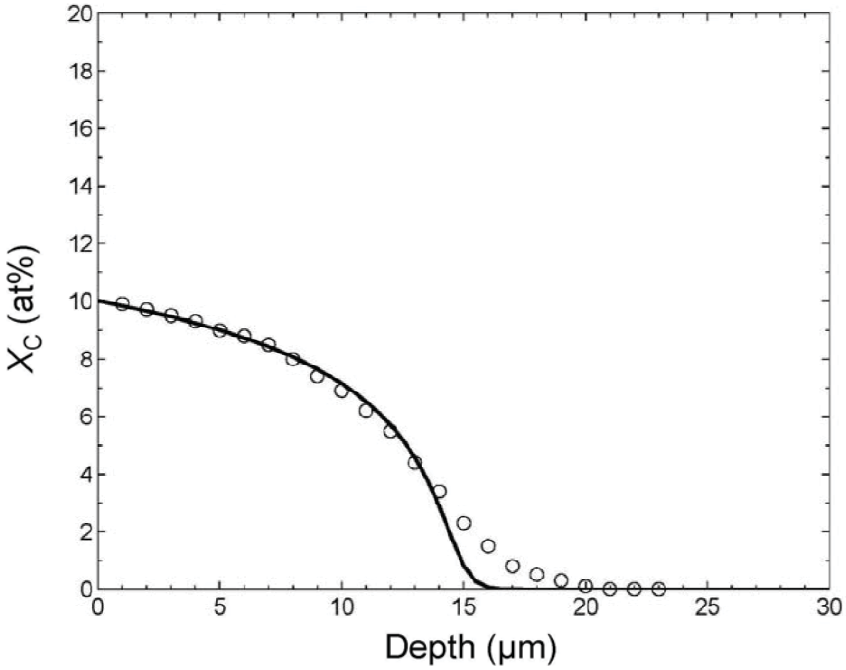

Figure 5. Simulated profile (solid line) for C15[C] and the experimental data (circles) taken from Figure 1.

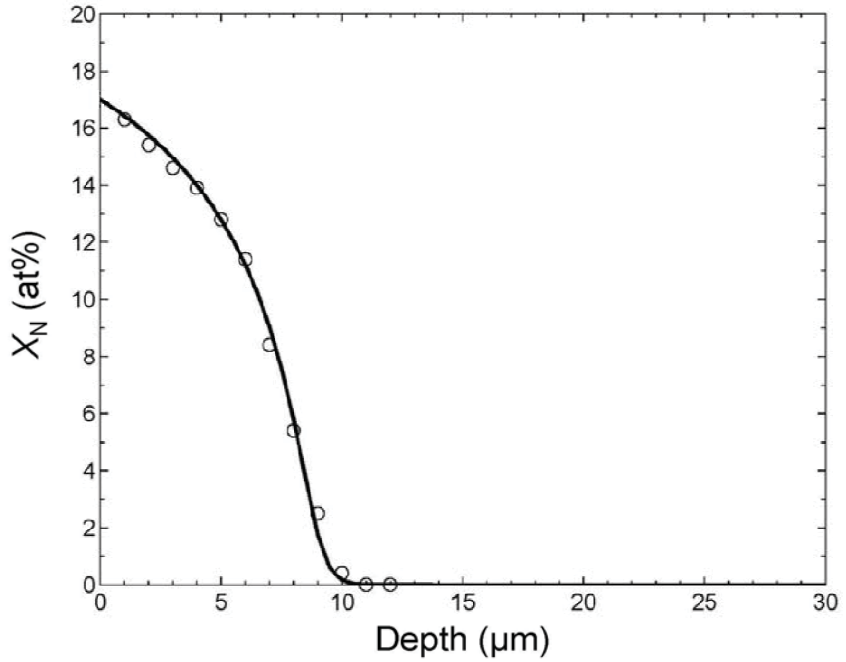

Figure 6. Simulated profile (solid line) for N15[N] and the experimental data (circles) taken from Figure 1.

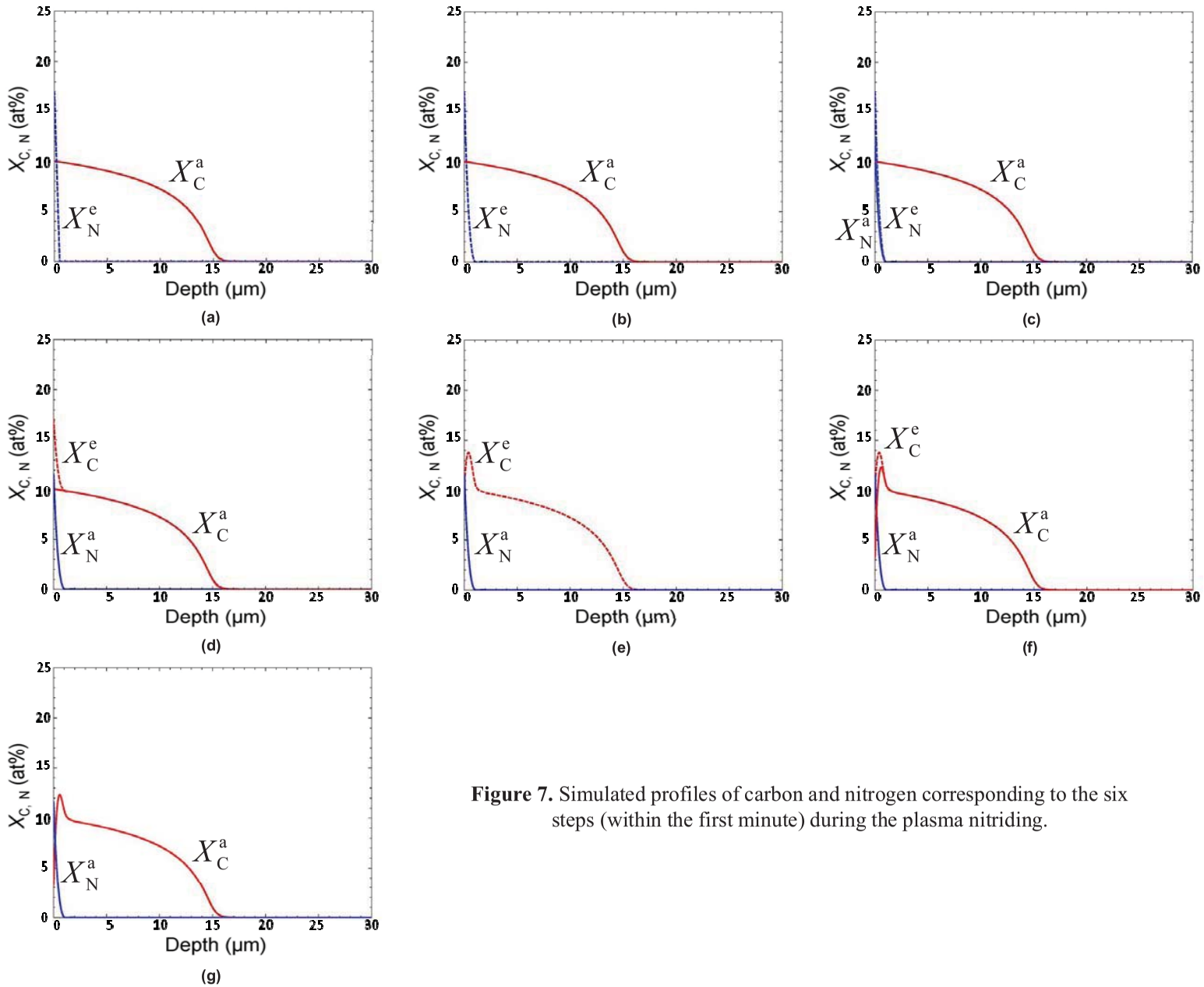

Figure 7. Simulated profiles of carbon and nitrogen corresponding to the six steps (within the first minute) during the plasma nitriding.

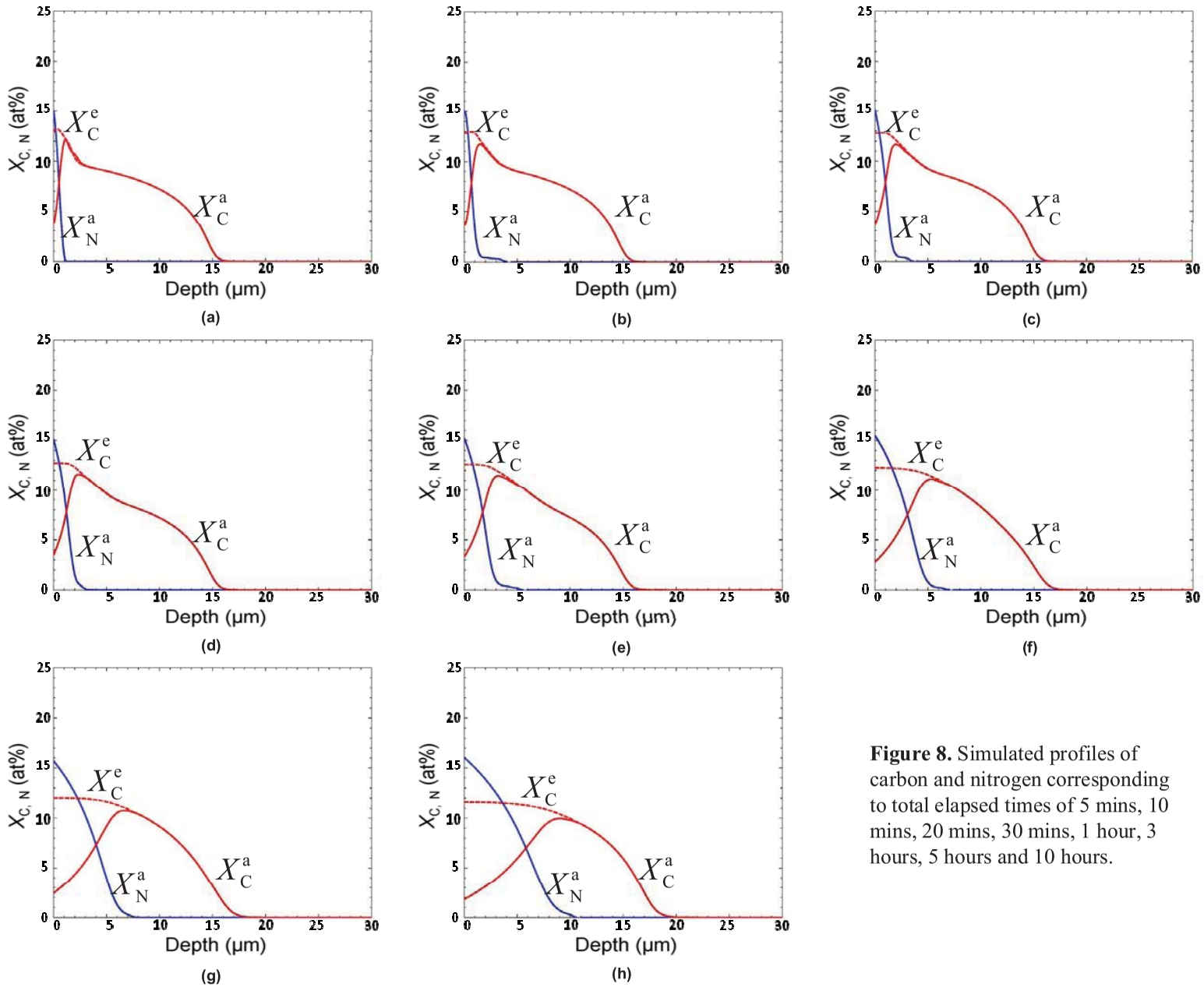

Figure 8. Simulated profiles of carbon and nitrogen corresponding to total elapsed times of 5 mins, 10 mins, 20 mins, 30 mins, 1 hour, 3 hours, 5 hours and 10 hours.

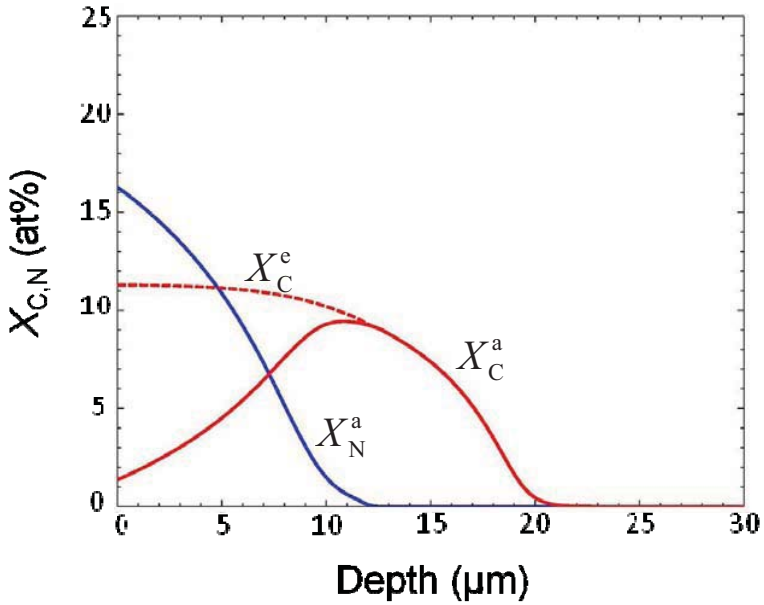

(a)

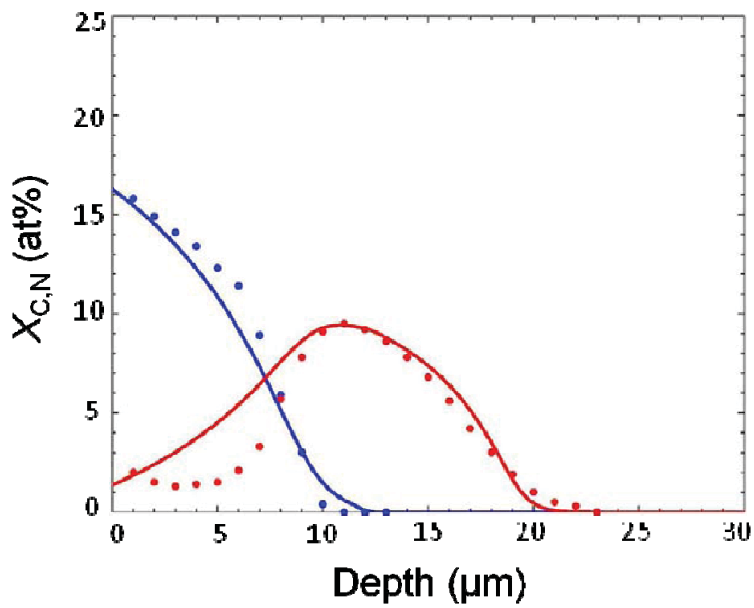

(b)

Figure 9. (a) The final simulated profiles X_C^a , X_C^e and X_N^a for a 430°C/30h plasma nitrocarburizing treatment. **(b)** Comparison of X_C^a and X_N^a (solid lines) with the experimental data (dots) for N15C15[C] and N15C15[N] as shown in Figure 1.

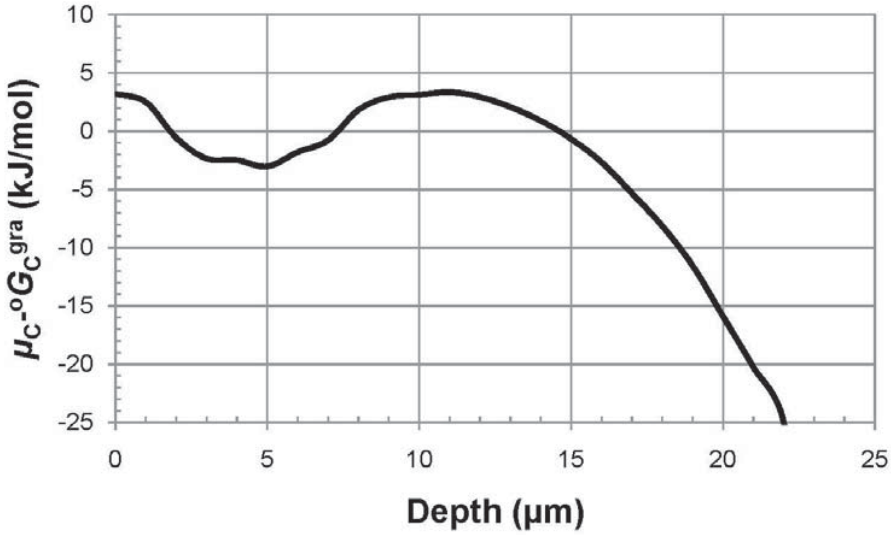

(a)

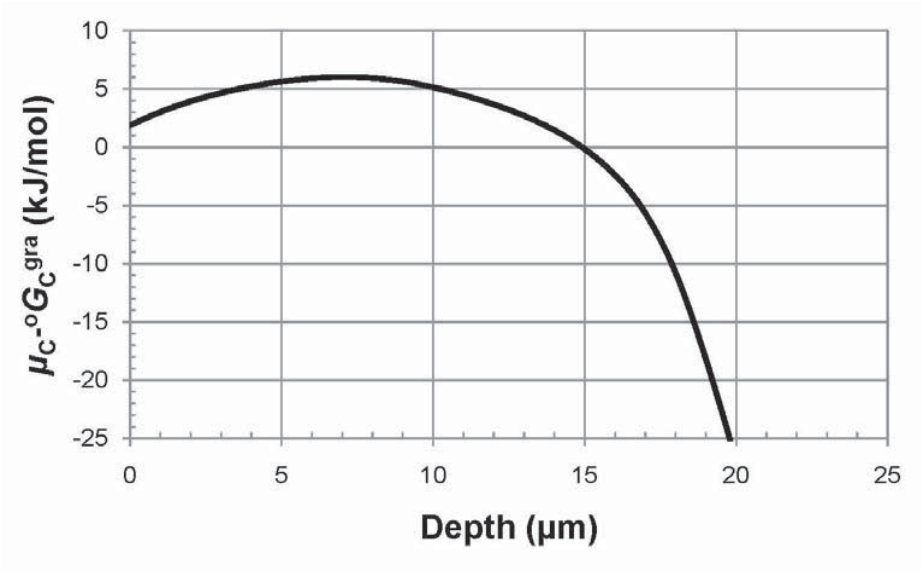

(b)

Figure 10. The final chemical potential profile of carbon relative to graphite for 430°C/30h plasma nitrocarburization based upon: **(a)** the experimental data in Figure 1, and **(b)** the simulation result in Figure 9(b).

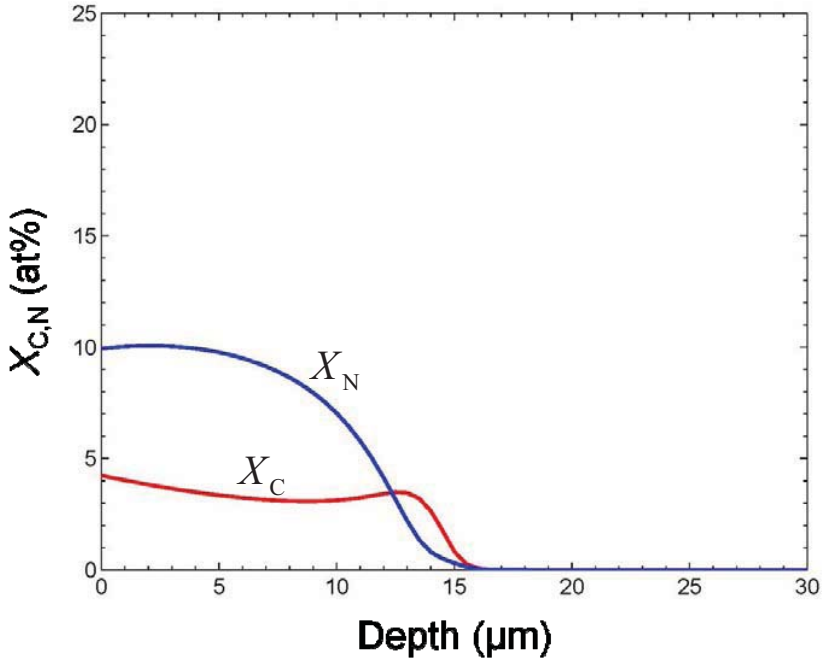

Figure 11. The simulated profiles of actual carbon and nitrogen concentrations for a 15-h plasma nitridation followed by a 15-h plasma carburization at 430°C.

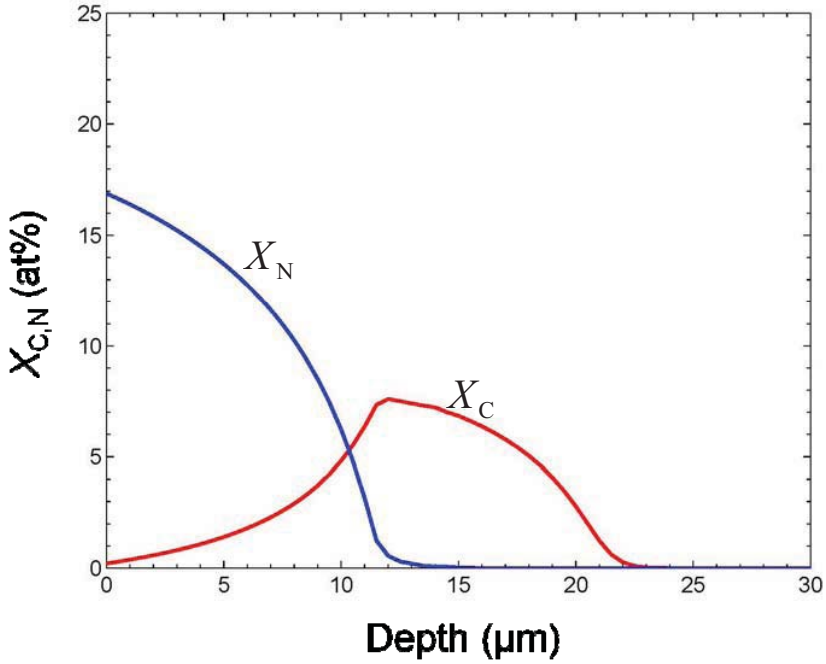

Figure 12. The simulated profiles of actual carbon and nitrogen concentrations for a 30-h simultaneous plasma nitrocarburizing process at 430°C.

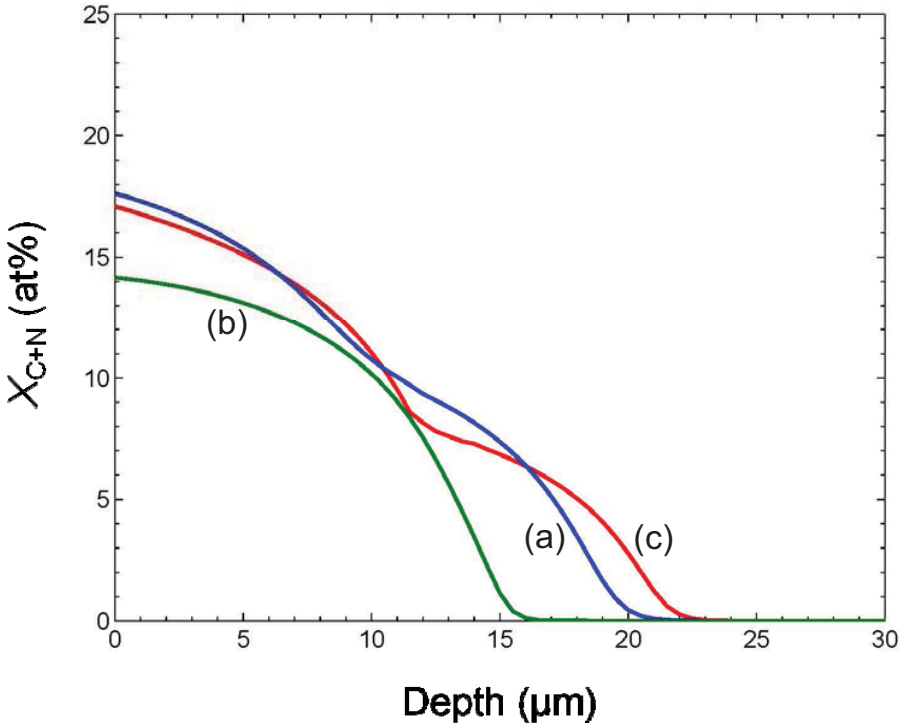

Figure 13. The simulated actual concentration–depth profiles of the total amount of carbon and nitrogen produced by the three different processes at 430°C: (a) 15-h plasma carburization followed by 15-h plasma nitridation, (b) 15-h plasma nitridation followed by 15-h plasma carburization, and (c) 30-h simultaneous plasma nitrocarburizing process.